

The annual-hydrogen-yield-climatic-response ratio: evaluating the real-life performance of integrated solar water splitting devices

Moritz Kölbach,^{*a,b,c} Oliver Höhn,^d Kira Rehfeld,^e Manuel Finkbeiner,^f James Barry,^{f,g} and Matthias M. May^{a,b}

^aUniversität Tübingen, Institute of Physical and Theoretical Chemistry, Tübingen, Germany.

^bUniversität Ulm, Institute of Theoretical Chemistry, Ulm, Germany.

^cHelmholtz-Zentrum Berlin für Materialien und Energie GmbH, Institute for Solar Fuels, Berlin, Germany.

^dFraunhofer ISE für Solare Energiesysteme, Freiburg, Germany.

^eUniversität Tübingen, Department of Geosciences and Department of Physics, Tübingen, Germany.

^fUniversität Heidelberg, Institute of Environmental Physics, Heidelberg, Germany.

^gInternational Centre for Sustainable Development, Hochschule Bonn-Rhein-Sieg, Sankt Augustin, Germany.

*Email Address: moritz.koelbach@uni-tuebingen.de

Abstract: Integrated solar water splitting devices that produce hydrogen without the use of power inverters operate outdoors and are hence exposed to varying weather conditions. As a result, they might sometimes work at non-optimal operation points below or above the maximum power point of the photovoltaic component, which would directly translate into efficiency losses. Up until now, however, no common parameter describing and quantifying this and other real-life operating related losses (e.g. spectral mismatch) exists in the community. Therefore, the annual-hydrogen-yield-climatic-response (AHYCR) ratio is introduced as a figure of merit to evaluate the outdoor performance of integrated solar water splitting devices. This value is defined as the ratio between the real annual hydrogen yield and the theoretical yield assuming the solar-to-hydrogen device efficiency at standard conditions. This parameter is derived for an exemplary system based on state-of-the-art AlGaAs//Si dual-junction solar cells and an anion exchange membrane electrolyzer using hourly resolved climate data from a location in southern California and from reanalysis data of Antarctica. This work will help to evaluate, compare and optimize the climatic response of solar water splitting devices in different climate zones.

1 Introduction

Hydrogen produced from renewable energy can contribute to the decarbonisation of those industry sectors that are hard or even impossible to electrify.³² The upscaling process for this greenhouse gas-free hydrogen production technology is currently dominated by electrolyzers powered with solar or wind energy. However, more integrated approaches such as photoelectrochemical (PEC) water splitting²⁸ or integrated photovoltaic-electrolysis systems^{5,15} could optimize hydrogen production due to lower balance of system costs. For example, these systems are intended to work without the use of power electronics. Moreover, higher integration is accompanied by the possibility to use the heat loss in the absorber as an efficiency boost via simultaneously enhancing the catalytic performance of the water splitting reactions, decreasing the Ohmic losses, and cooling the absorber.^{19,25,29}

Whereas the installation and commissioning of electrolyzers in the multi-MW range is already ongoing in several countries, more integrated approaches still suffer from a low technology readiness level (TRL). While lab-scale PEC devices based on III-/V dual-junction absorbers are reaching solar-to-hydrogen (STH) efficiencies of up to 19.3%,⁷ the high material costs, non-trivial upscaling and long-term stability currently hinder practical applications. Integrated photovoltaic-electrolysis (PV-electrolysis) systems, in which the absorber is not directly immersed in the electrolyte exhibit a higher TRL due to better stability and more straightforward scalability.⁵ A reason for the relatively low TRL of both approaches compared to the completely decoupled approach, however, is that these systems are intended to operate outdoors without a power inverter. While this on the one hand represents an advantage with respect to costs, maintenance, and efficiency (no losses in the inverter), it implies that these devices are exposed to varying weather conditions (e.g. ambient temperature). Recently, Reuß et al. performed a bottom-up analysis of different device configurations and argued that systems with no power inverter have the disadvantage of not always operating at the maximum power point (MPP) of the photovoltaic module component.²⁶ Therefore, integrated devices might

in the end be less efficient with respect to the annual hydrogen yield than the completely decoupled approach using power inverters, even with the associated efficiency losses of around 5%. Moreover, it is argued that integrated devices might have to be customized for each production location to maximize the annual hydrogen yield - a major drawback for potential mass production.

Efforts to understand the effects of varying weather conditions on integrated water splitting devices on a yearly basis have only started recently.^{3,17,37,38} For example, Kemppainen et al. investigated the effect of ambient conditions on the operation of thermally coupled PV-electrolysis systems based on silicon heterojunction photovoltaic cells and an alkaline electrolyzer.¹⁷ For this device, an STH efficiency ranging between 3.4 and 10% was found, which was mainly influenced by the device operating temperature. This rather large efficiency range emphasizes the need for a deeper understanding and evaluation of the climatic response of such systems. Furthermore, Pehlivan et al. modelled the climatic response of single junction Si and CIGS solar cells connected in series with thermally integrated electrolyzers. They found that the STH efficiency can be more or less retained over a full year using total spectral irradiance and ambient temperature data from a mid-European location (Jülich, Germany).³ It was shown that the reduced power output from the solar cells at low irradiation could be counterbalanced by the lower overpotential required for the catalysts. Finally, Welter et al. investigated the influence of simulated outdoor illumination conditions on the performance of various solar water splitting systems.³⁷ They highlighted the influence of the incident illumination angle on the efficiency and estimated the long-term hydrogen generation depending on the annual average photon energy (*APE*) of the solar spectra for an example location.

For high efficiency solar water splitting devices that potentially exceed efficiencies of 20%, multi-junction photoabsorbers are required in order to reduce thermalization and transmission losses in the absorbers.^{7,21} In the PV community, such multi-junction solar cells based on Si bottom absorbers are currently being investigated with the aim to end the dominance of single-junction Si solar cells in the PV market.⁴ Wide-bandgap III/V-semiconductors⁶ or perovskites^{1,14} are considered as potentially economically viable candidates to be used as top absorbers. In addition, all-perovskite multi-junctions are also regarded as promising material combinations.¹³ All these multi-junction structures can in principle be regarded as potential photoabsorbers in solar water splitting devices. Note that for PEC devices, only dual-junctions have the potential to yield STH efficiencies beyond 20%, while integrated PV-electrolysis systems with a similar or even higher efficiency can also be based on triple junctions.¹⁵ The use of multi-junctions in solar water splitting devices does, however, even further increases the complexity level of their climatic response. Since the absorbers are stacked and connected in series, deviations from the AM1.5g spectrum in real-life outdoor operation conditions (e.g. due to clouds) can lead to a current mismatch in the absorber. This would directly translate into a reduction of the photocurrent, and hence the efficiency. For photovoltaic solar cells, this current mismatch increases the fill factor (FF) of a subcell and hence counterbalances the efficiency losses at least to some extent.¹⁸ This could be different for solar water splitting devices, since the operation point is defined by the intersection of the catalyst and solar cell IV curve and not by a MPP tracker.

The considerations above emphasize the need for a deeper understanding of the climatic response of integrated solar water splitting systems - especially when multi-junction solar cells are used. To the best of our knowledge, however, there is no common definition of a parameter describing and quantifying the climatic response of these systems in the community.

Here, we introduce the annual-hydrogen-yield-climatic-response (AHYCR) ratio as a figure of merit for the evaluation of the real-life performance of integrated solar water splitting devices. This parameter is defined as the ratio between the real annual hydrogen yield and the theoretical yield assuming STH efficiency at standard conditions. We derive this parameter for a water splitting device consisting of state-of-the-art AlGaAs//Si dual-junction solar cells and a thermally coupled anion exchange membrane (AEM) electrolyzer via modelling the annual hydrogen yield based on hourly resolved climate data. The input data for the model contains the solar spectrum (direct and diffuse parts), the ambient temperature, the panel tilt/azimuth angle, as well as the solar zenith/azimuth angle. As example locations with very contrasting climate conditions, the climatic response of the device operating in southern California and near the German polar research station “Neumayer” in Antarctica is modelled. Our work allows to assess the requirement for specific adaptation of highly integrated solar water splitting systems to the climatic boundary conditions of a given location.

2 Annual hydrogen yield modelling

Fig. 1 shows a sketch of the modelled integrated solar water splitting device configuration in this study. It consists of a wafer-bonded AlGaAs//Si dual-junction solar cell as the photovoltaic component, which is electrically directly connected and thermally coupled to an AEM electrolyzer. In addition, the surface normal of the device, the solar incidence angle Θ of the direct sunlight, and the diffuse illumination are indicated. The inset shows the solar cell module stack used for the optical modelling in more detail.

The flowchart of our model that predicts the annual hydrogen yield for our system is shown in Fig. 2. This Python-based model is part of the YaSoFo software package^{20,21} and the code is published alongside this manuscript. As hourly resolved input parameters, the geometry of the system (device tilt/azimuth angle and solar zenith/azimuth

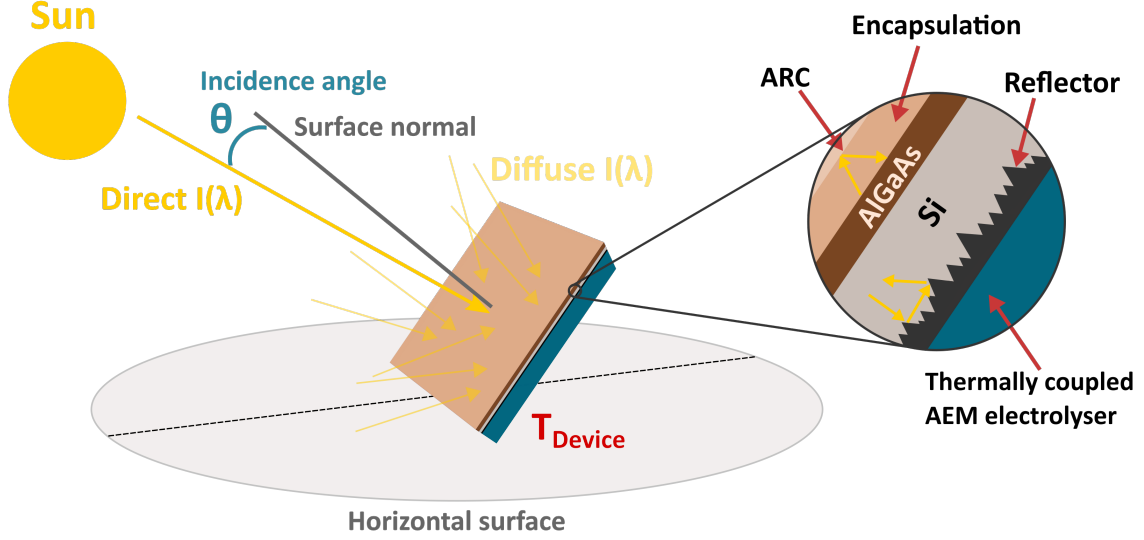


Fig. 1: Sketch of the solar water splitting device based on an AlGaAs//Si dual-junction solar cell directly electronically connected and thermally coupled to an AEM electrolyzer. The surface normal, incidence angle, as well as direct and diffuse irradiation are indicated. Inset: Sketch of the simulated solar cell module stack of the encapsulated dual-junction with random pyramids coated with a silver mirror for light trapping and an anti-reflection coating (ARC) on the surface.

angle), the ambient temperature, as well as the solar spectrum (direct and diffuse parts) impinging on the device are used as input parameters (yellow box).

First, the model calculates the angle of incidence (Θ) from the device tilt angle, the device azimuth angle, the solar azimuth, and the solar zenith angle using the *pvl* Python-package.¹¹ The operating temperature of the device is then estimated from the global irradiance I using the following simple empirical equation:¹²

$$T_{\text{device}} = I \cdot 0.025 \text{ [K m}^2 \text{ W}^{-1}] + T_{\text{ambient}}. \quad (1)$$

Next, the external quantum efficiency (EQE) in both the AlGaAs and Si junction for direct irradiation is obtained from the angle of incidence and the device temperature using the OPTOS formalism.^{12,30,31} With this formalism, the absorbance, reflectance, and transmittance of the incident light across all layers of the module stack (see zoom in in Fig. 1) can be modelled. The temperature dependence of the EQE is obtained using the bandgap shift model.² For this, the temperature-dependent bandgap (E_g) of Si is calculated using the Varshni relation,³³

$$E_g = E_{g,0} - \frac{\alpha T^2}{\beta + T}, \quad (2)$$

where $E_{g,0}$ is the bandgap at absolute zero and α as well as β are material constants. For Silicon, $E_{g,0} = 1.166 \text{ eV}$, $\alpha = 4.73 \times 10^{-4} \text{ eV K}^{-1}$, and $\beta = 636 \text{ K}$ are used.²⁷ In the case of AlGaAs, parameters extracted from reference³⁵ are employed to calculate the temperature and composition dependent bandgap. The temperature-dependent EQE in both junctions for diffuse irradiation is estimated using the following equation, which weights the EQEs for discrete angles obtained from OPTOS over their corresponding angle of incidence under the summation:¹²

$$EQE_{\text{diffuse}} = \frac{\sum EQE(\Theta) \cdot \cos(\Theta) \cdot \sin(\Theta)}{\sum \cos(\Theta) \cdot \sin(\Theta)}. \quad (3)$$

Note that this formula assumes an isotropic sky for the sake of simplicity. The temperature-dependent IV characteristic of the dual-junction is obtained from the 2-diode model in each series-connected subcell. The implicit 2-diode equation is given as follows:

$$j = j_{\text{ph}} - j_{01} \left[\exp \left(\frac{q(V + jR_s)}{k_b T} \right) - 1 \right] - j_{02} \left[\exp \left(\frac{q(V + jR_s)}{2k_b T} \right) - 1 \right] - \frac{V + jR_s}{R_p}. \quad (4)$$

Here, j_{ph} is the photocurrent density, j_{01} and j_{02} are the saturation current densities, q is the electronic charge, V is the voltage, R_s is the series resistance, k_b is the Boltzmann constant, and R_p is the parallel resistance. The photocurrent

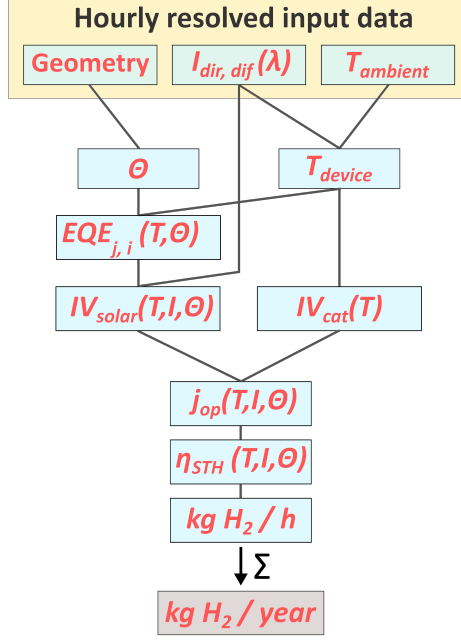


Fig. 2: Flow chart of the modelling procedure to determine the annual hydrogen yield of the thermally coupled solar water splitting device.

in each junction is calculated as the sum of the generated photocurrent for the direct and diffuse illumination from the corresponding EQEs and the solar spectra. The temperature dependence of the saturation current densities can be obtained using the Wannlass model from the Wannlass Parameters A_{01} , B_{01} , and β_{02} as follows:³⁶

$$j_{01} = A_{01} \exp(B_{01} E_g(T)) T^3 \exp\left(-\frac{E_g(T)}{k_b T}\right) \quad (5)$$

$$j_{02} = \beta_{02} T^{\frac{5}{2}} \exp\left(-\frac{E_g(T)}{2k_b T}\right). \quad (6)$$

The total IV curve of the dual-junction solar cell can then be obtained from the individual IV characteristics of the series-connected subcells. The temperature dependence of the IV curve of the electrolyzer is modelled based on the device temperature and a set of experimental temperature-dependent input data, which is fitted with a routine employing the Lambert W function using the equation:

$$j_{\text{catalysts}} = \frac{S_{\text{Tafel}}}{R_{\text{Ohm}}} \cdot W \left[\frac{j_0 R_{\text{Ohm}} \exp\left(\frac{U - \Delta G}{S_{\text{Tafel}}}\right)}{S_{\text{Tafel}}} \right]. \quad (7)$$

Here, S_{Tafel} is the effective Tafel slope in $[\text{V dec}^{-1}]$, j_0 is the effective exchange current density, ΔG is the Gibbs free energy of the redox reaction, and R_{Ohm} is the ohmic resistance of the cell. The temperature dependence of the ohmic cell resistance is calculated from the effective electrode distance d , the reference membrane conductivity $\kappa_{0, \text{mem}}$, the membrane activation energy $E_{a, \text{mem}}$, and the the universal gas constant R as follows:¹⁰

$$R_{\text{Ohm}} = \frac{d}{\kappa_{0, \text{mem}} \exp\left(\frac{-E_{a, \text{mem}}}{RT}\right)}. \quad (8)$$

The influence of the temperature on j_0 is considered in the fitting routine via the following equation,

$$j_0 = j_{0, T_{\text{ref}}} \exp\left[\frac{E_a}{R} \left(\frac{1}{T_{\text{ref}}} - \frac{1}{T}\right)\right], \quad (9)$$

where $j_{0, T_{\text{ref}}}$ is the exchange current density at the reference temperature, and E_a is the effective activation energy. The temperature dependence of ΔG is given by the following simple relationship:

$$\Delta G = 1.4746 [\text{V}] - 0.0008212 [\text{V K}^{-1}] \cdot T [\text{K}]. \quad (10)$$

The intersection of the IV characteristics of the solar cells and the electrolyzer represents the operation current density j_{op} of the device. From this, and the total spectral irradiance impinging on the device I , the STH efficiency η_{STH} is calculated as follows:

$$\eta_{\text{STH}} = 100\% \cdot \frac{j_{\text{op}} [\text{A m}^{-2}] \cdot 1.23 [\text{V}]}{I [\text{W m}^{-2}]} . \quad (11)$$

From the Avogadro constant N_{A} , and the molar mass of hydrogen M_{H_2} the hourly hydrogen yield can be calculated using the following expression:

$$H_{2, \text{ hourly yield}} = \frac{j_{\text{op}} M_{\text{H}_2} \cdot 3600 [\text{s h}^{-1}]}{2qN_{\text{A}}} . \quad (12)$$

Finally, the sum of the hydrogen yield for each hour gives the total annual hydrogen yield ($H_{2, \text{ real AY}}$) of the device:

$$H_{2, \text{ real AY}} [\text{kg a}^{-1} \text{ m}^{-2}] = \sum_{i=1}^{8760} H_{2, \text{ hourly yield}} [\text{kg h}^{-1} \text{ m}^{-2}] . \quad (13)$$

For a more detailed description of the model we refer the reader to the documentation of the Python-Code published alongside this work.²⁰

Table 1 and Table 2 contain the input parameters for the dual-junction solar cell and the AEM electrolyzer used in this work, respectively. The parameters for the AlGaAs and Si cells were obtained from literature.¹² The parameters for the AEM electrolyzer are based on the temperature-dependent experimental data from Vincent et al.³⁴ and are extracted using the fitting routine described above (see Fig. S1 in the SI). The x in $\text{Al}_x\text{Ga}_{1-x}\text{As}$ was set to 0.19 which translates into a top absorber bandgap of 1.70 eV at 25°C. This value was obtained via optimizing the system with respect to its STH efficiency for standard conditions, i.e. AM1.5g illumination and a device temperature of 25°C (see Fig. S2 in the SI). The $\text{Al}_{0.19}\text{Ga}_{0.81}\text{As}$ top cell is from now on referred to as AlGaAs.

Table 1: Input parameters for the AlGaAs and Si junction¹²

Parameter	Symbol	AlGaAs top cell	Si bottom cell	Unit
Series resistance	R_{s}	0.1030	0.1035	$\Omega \text{ cm}^2$
Parallel resistance	R_{p}	1×10^3	5×10^3	$\Omega \text{ cm}^2$
Wannlass parameter	A_{01}	0.088	1.267	$\text{mA cm}^{-2} \text{ K}^{-3}$
Wannlass parameter	B_{01}	1.625	1.625	eV^{-1}
Wannlass parameter	β_{02}	0.040	1.507×10^{-3}	$\text{mA cm}^{-2} \text{ K}^{-2.5}$

Table 2: Fitted input parameters for the AEM electrolyzer³⁴

Parameter	Symbol	Fitted value	Unit
Effective Tafel slope	S_{Tafel}	44.0	mV dec^{-1}
Electrode distance	d	0.0212	cm
Effective exchange current density at 298 K	j_0, T_{ref}	5.92×10^{-7}	A cm^{-2}
Effective activation energy	E_{a}	54.9	kJ mol^{-1}
Reference membrane conductivity	κ_0, mem	62.1	mS cm^{-1}
Activation energy membrane	$E_{\text{a, mem}}$	2.85	kJ mol^{-1}

2.1 Temperature dependence of the solar cell and electrolyzer IV characteristics

The modelled temperature-dependent IV characteristics of the AlGaAs//Si dual-junction and the AEM electrolyzer are shown in Fig. 3. For the IV curves of the dual-junction, AM1.5g illumination and normal incidence ($\Theta = 0$) were assumed. The two well-known contrary effects of temperature on the solar cell and electrolyzer IV characteristics are visible. For the electrochemical component, an increased temperature is beneficial due to higher catalytic activity, lower ΔG , and reduced ohmic losses. In other words, a lower potential has to be applied at a higher operating temperature to obtain the same current density for the overall water splitting reaction. For the solar cell, however, the efficiency decreases with increasing temperature due to a decreasing open circuit potential (VOC) with increasing operation temperature. For our AlGaAs//Si solar cell, a reasonable VOC temperature coefficient of -0.202 \% K^{-1} is extracted (see Fig. S3 in the SI). The slight increase of the short circuit current density for higher temperatures results from the decreasing bandgap energy of the AlGaAs and Si semiconductors (see Fig. S4 in the SI). This causes a shift of the total EQE towards higher wavelengths and hence a higher photocurrent in both junctions (see Fig. S5 in the SI).

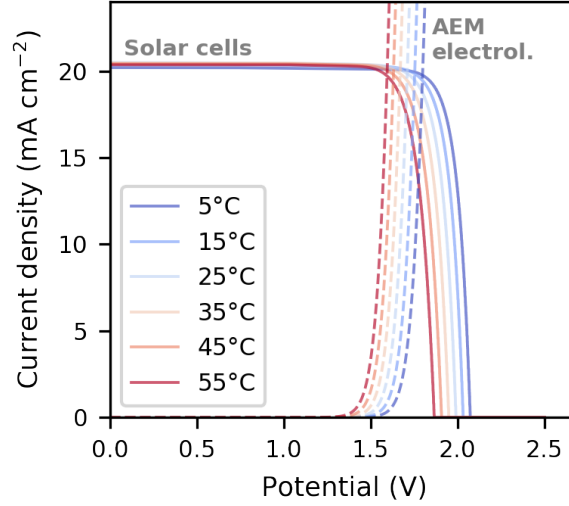


Fig. 3: Influence of the operating temperature in the range from 5 to 55°C on the IV characteristics of the AEM electrolyzer and the AlGaAs//Si dual-junction. The solar cell IV curves were modelled assuming AM1.5g illumination and an angle of incidence equal to 0°.

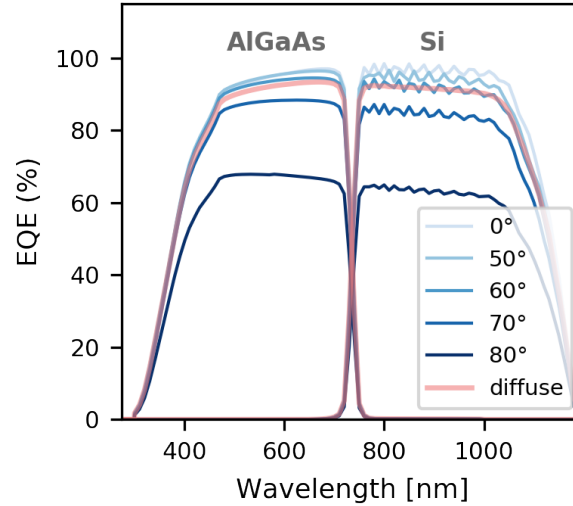


Fig. 4: Influence of the incidence angle on the external quantum efficiency of the AlGaAs//Si dual-junction for a device temperature of 25°C.

The operation point of the solar water splitting device is determined by the intersection of both IV curves. In the temperature range considered here, the contrasting temperature effects almost cancel each other out, resulting in a relatively constant operation current density for our example device. Note that this observation cannot be generalized and depends on a number of parameters such as for example the ohmic resistance of the electrochemical component and could also change, if other temperature ranges are considered.^{17,19}

2.2 Incidence angle dependence of the EQEs

The influence of the angle of incidence of direct irradiation on the EQEs in the AlGaAs and Si cell modelled with the OPTOS formalism^{30,31} is shown in Fig. 4 (blue colors). The device temperature was set to 25°C. It can be seen that both EQEs only slightly decrease with increasing angle of incidence until a value of 60°, after which the EQEs start to drop significantly. The EQEs calculated for diffuse irradiation using equation (3) is also shown.

2.3 Climatic input data

Fig. 5a shows the two example locations considered in this study: southern California (34.01°/-116.7°, location 1) and near the Neumayer station in Antarctica (-70.67°/-8.28°, location 2), a location that was already chosen in a recent study proposing the use of thermally coupled solar water splitting devices for hydrogen production in cold

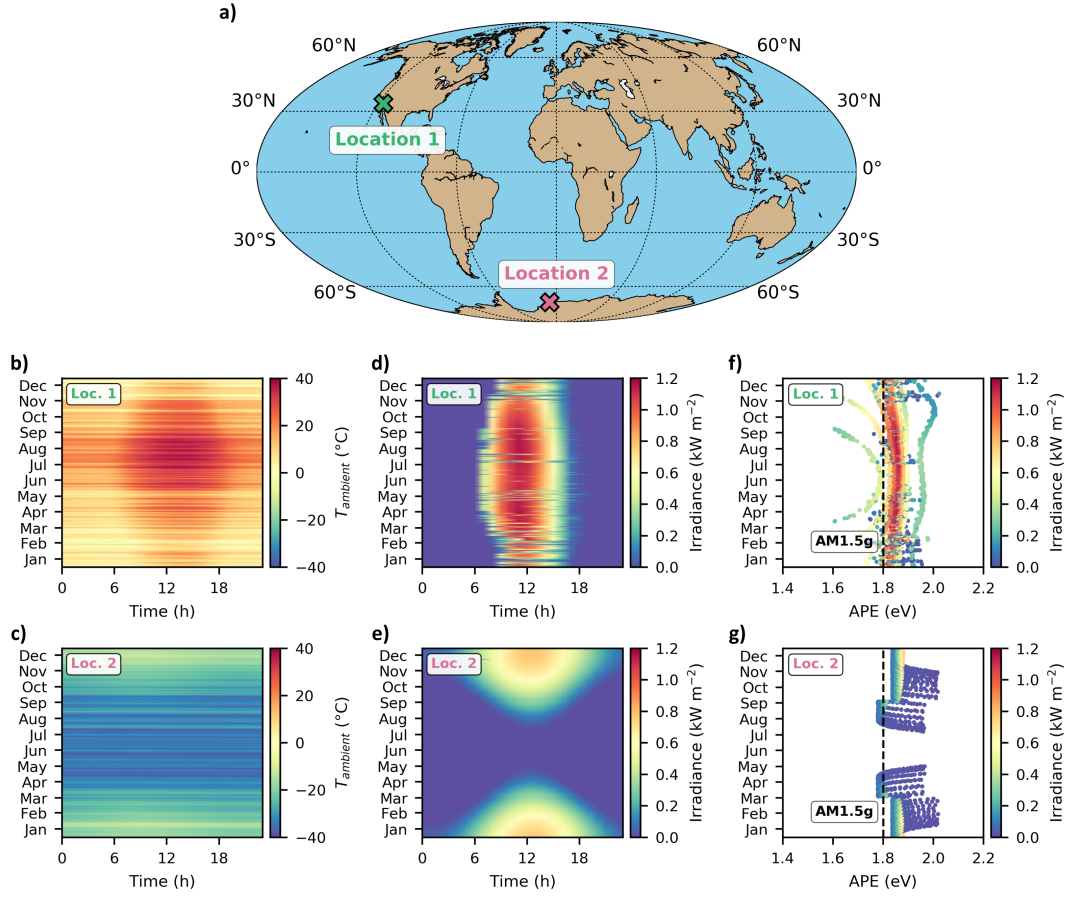


Fig. 5: Climatic data at a location in southern California ($34.01^{\circ}/-116.7^{\circ}$, year 2019) and in Antarctica ($-70.67^{\circ}/-8.28^{\circ}$, year 2021). (a) World map indicating both locations. (b), (c) Hourly resolved annual ambient temperature. (d), (e) Hourly resolved annual total spectral irradiance impinging on the device. (e), (f) Distribution of the hourly resolved average photon energy in a wavelength regime from 280 to 1200 nm. The dashed vertical line indicates the average photon energy of the AM1.5g spectrum.

regions.¹⁹ Hourly resolved data for location 1 was obtained from NREL’s spectral on-demand database^{39–41} for the year 2019. It inter alia contains the solar spectrum, the ambient temperature, as well as the solar zenith and azimuth angle. The panel tilt and azimuth angle were set to 40° and 130°, respectively. Note that the hourly resolved data from NREL’s database only contains the global spectrum impinging on the panel and does not differentiate between direct and diffuse light. However, the absolute irradiance for the DNI and DHI are given, from which the fraction of the diffuse light of the total spectral irradiance impinging on the device can be obtained. For this location, the same spectrum for both direct and diffuse irradiance is therefore assumed as an approximation as suggested recently.¹² The hourly resolved solar spectra for direct and diffuse radiation at location 2 were modelled using the libRadtran software package employing the predefined "subarctic summer" and "subarctic winter" atmosphere datasets for the year 2021.^{8,22,23} For the sake of simplicity, a clear sky (no cloud cover) is assumed over the course of the whole year. In the model, the panel tilt angle was set to 70° and 1-axis tracking was assumed, i.e., the panel azimuth angle equals the solar azimuth angle. Hourly resolved ambient temperature reanalysis data for the year 2021 was obtained from the ERA5 reanalysis product.¹⁶ Note that this represents a first approximation. A more detailed study including for example the effect of clouds is left for future work.

The hourly resolved annual ambient temperature for southern California and Antarctica is shown in Fig. 5b and c, respectively. With an average annual ambient temperature of 14.4°C and −27.2°C, the two locations represent very contrasting climatic conditions. Note that the modelling in this work neglects potential device operating failures due to extreme cold temperatures. However, it was shown that the right choice of an electrolyte that sufficiently depresses the freezing point of water enables solar water splitting far below 0°C.¹⁹ The hourly resolved total spectral irradiance impinging on the device for both locations is shown in Fig. 5d and e. The typical daily and annual course of the irradiance in a subtropical climate zone on the northern hemisphere and the antarctic polar zone are clearly visible. The total annual spectral irradiance impinging on the panel equals to 2316.95 kWh m^{−2}a^{−1} and 1272.35 kWh m^{−2}a^{−1} for the location in southern California and Antarctica, respectively.

Fig. 5f and g illustrate the hourly resolved irradiance data with respect to the average photon energy (*APE*) from 280 to 1200 nm for location 1 and 2, respectively, defined as follows:

$$APE = \frac{\int I(\lambda) d\lambda}{\frac{q}{hc} \int I(\lambda) \lambda d\lambda}. \quad (14)$$

Here, h is the Planck constant, c is the speed of light, and λ is the wavelength of the photon. This value is typically used in the PV community to initially evaluate deviations from the AM1.5g spectrum under real-life conditions. For both locations, the spectra tend to have higher APE values compared to the AM1.5g spectrum, which has an APE of 1.8 eV in this wavelength regime (vertical dashed lines in Fig. 5f and g). This would generally translate into a current mismatch in the dual-junction, which was initially optimized to the AM1.5g spectrum. In this case, the photocurrent in the front absorber would be too high and the bottom absorber would limit the overall photocurrent. However, it can be seen that in both cases large deviations coincide with lower irradiance and that for high irradiance, the APE is close to the AM1.5g reference. This reduces the impact of the spectral mismatch on the annual hydrogen yield as discussed later in detail. Note that the steps visible in Fig. 5g are a result of the switch between the “subarctic summer” and “subarctic winter” atmosphere datasets. The climatic and geometric input parameters for both locations are summarized in Table 3.

Table 3: Summary of climate and geometric input parameter

Parameter	Location 1 (Southern California)	Location 2 (Antarctica)
Lat./Long.	34.01°/−116.7°	−70.67°/−8.28°
Panel tilt angle	40°	70°
Panel azimuth angle	130°	1-axis tracking
Year	2019	2021
Annual $T_{\text{ambient, avg}}$	14.4°C	−27.2°C
Annual I_{panel}	2316.95 kWh m ^{−2} a ^{−1}	1272.35 kWh m ^{−2} a ^{−1}
Annual APE ($I > 100 \text{ Wm}^{-2}$)	1.852 eV	1.853 eV

3 Results & discussion

3.1 Climatic response of the device in southern California

Fig. 6 shows the hourly resolved modelling results for the location in southern California. As discussed above, integrated solar water splitting devices without a power inverter might not always operate at the maximum power point (MPP) of

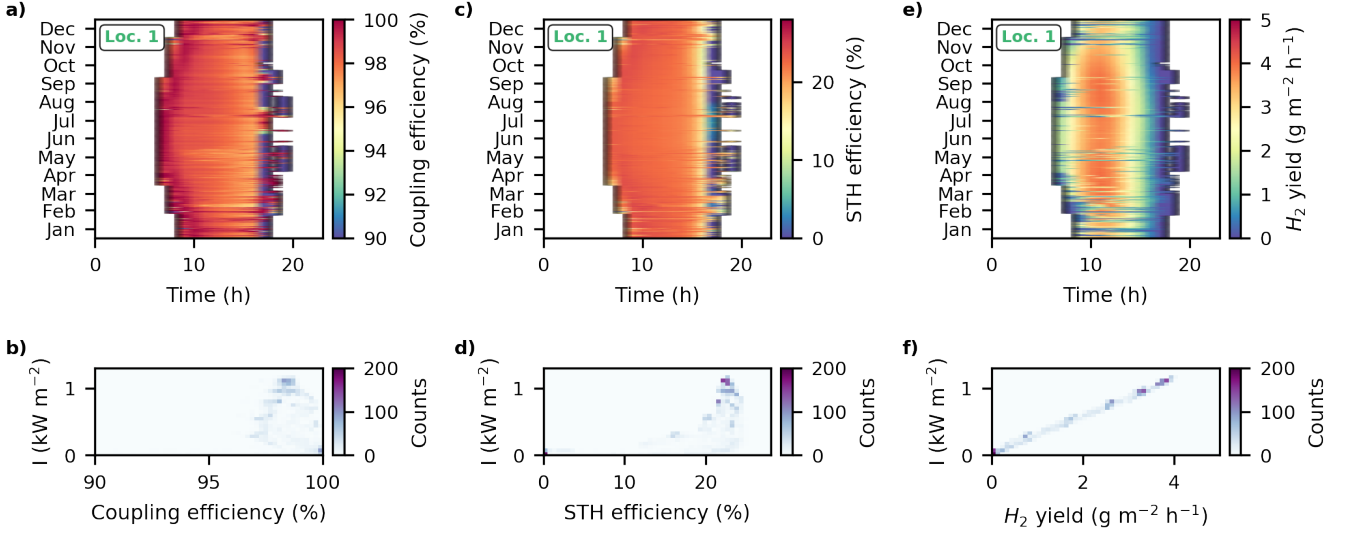


Fig. 6: Modelled climatic response of the solar water splitting device based on an AlGaAs//Si dual-junction and an AEM electrolyzer for the location in southern California. (a) Hourly resolved annual coupling efficiency. (b) 2D histogram of the coupling efficiency with regard to the total spectral irradiance impinging on the device. (c) Hourly resolved annual STH efficiency. (d) 2D histogram of the STH efficiency and the total spectral irradiance. (e) Hourly resolved annual hydrogen yield. (f) 2D histogram of the hydrogen yield and the total spectral irradiance.

the photovoltaic component, which would be accompanied by efficiency losses. To quantify this, Reuß et al. introduced the so-called “coupling efficiency” (η_{coupling}).²⁶ This value is defined as the ratio between the product of the operation current density and operation potential (E_{op}) of the solar water splitting device and the product of the current (j_{MPP}) and potential (E_{MPP}) at the MPP of its photovoltaic component:

$$\eta_{\text{coupling}} = 100\% \cdot \frac{j_{\text{op}} E_{\text{op}}}{j_{\text{MPP}} E_{\text{MPP}}} . \quad (15)$$

Coupling efficiencies lower than 100% imply that the device is not working at the optimum operation point of the photovoltaic component. For operation potentials higher than the MPP potential, the STH efficiency significantly drops due to a sharp decline of the photocurrent in this regime. When the operation potential is lower than the MPP potential, the STH efficiency does not significantly change. However, power is wasted via transformation into heat. Note that this heat can increase the operation temperature of the device and hence influence the STH efficiency. In this work, however, this effect is neglected since the area for heat dissipation is rather high in these devices and the operating temperature is mostly defined by the ambient temperature and irradiance.¹⁹ Fig. 6a and b show the hourly resolved annual coupling efficiency and the corresponding 2D histogram with regard to the total spectral irradiance, respectively. It can be seen that for our example device and location, the coupling efficiency is surprisingly constant. Over the course of the whole year, the coupling efficiency is almost always higher than 95%. This implies that all effects due to variable weather conditions on the IV characteristics of the solar cells and the electrolyzer cancel each other out, resulting in an operation close to MPP of the photovoltaic component. In the 2D histogram, no trend of the coupling efficiencies with respect to the total spectral irradiance can be observed.

Similar to the coupling efficiency, the hourly resolved annual STH efficiency shown in Fig. 6c is relatively constant over the course of the whole year reaching a value of around 22.5%. Lower STH efficiencies coincide with low irradiances, as can be seen in the 2D histogram shown in Fig. 6d, so that the impact on the annual energy yield should be rather low. This dependency is probably caused by the higher current mismatch in the dual-junction due to higher APE values of the spectra corresponding to low total spectral irradiances (see Fig. S6 in the SI and Fig. 5f). Fig. 6e finally shows the hourly resolved hydrogen yield. As expected from the relatively constant coupling and STH efficiency, the hydrogen yield linearly scales with the total spectral irradiance as shown in the 2D histogram in Fig. 6f. In total, the device produces $7.84 \text{ kg m}^{-2} \text{ a}^{-1}$ of hydrogen.

3.2 Climatic response of the device in Antarctica

Fig. 7 shows the analogous plots for the device operating in Antarctica. Similar to the operation in southern California, the system shows a relatively constant coupling efficiency with values higher than 96% (see Fig. 7a and b). Also the STH efficiency reveals a similar behaviour. A relatively constant efficiency of around 22.5% over the whole course of the year (see Fig. 7c) and a coincidence of lower efficiencies with lower total spectral irradiances (see Fig. 7d) are found. The latter is probably again caused by a higher current mismatch in the dual-junction due to higher APE

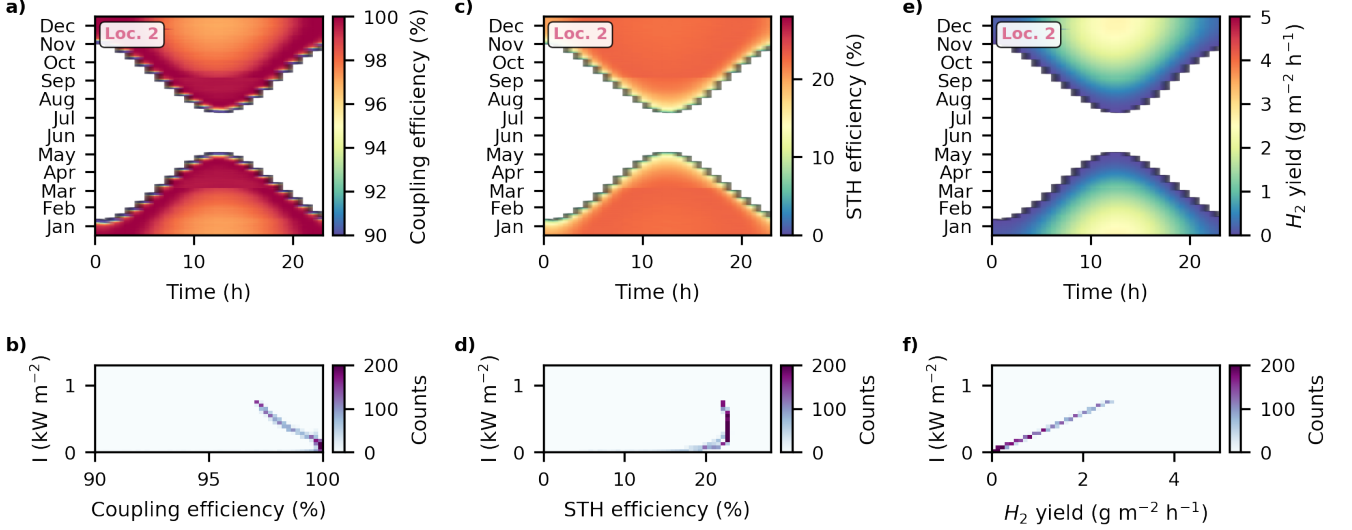


Fig. 7: Modelled climatic response of the solar water splitting device near the Neumayer station in Antarctica. (a) Hourly resolved annual coupling efficiency. (b) 2D histogram of coupling efficiency with respect to the total spectral irradiance impinging on the device. (c) Hourly resolved annual STH efficiency. (d) 2D histogram of the STH efficiency and the total spectral irradiance. (e) Hourly resolved annual hydrogen yield. (f) 2D histogram of the hydrogen yield and the total spectral irradiance.

values of the spectra corresponding to low total spectral irradiances (see Fig. S7 in the SI and Fig. 5g). As a result of the constant STH efficiency, the hydrogen yield again linearly scales with the total irradiance as can be seen in Fig. 7e and f. In total, the device produces $4.34 \text{ kg m}^{-2} \text{ a}^{-1}$, which is a bit more than half of the yield as found in southern California.

3.3 The annual-hydrogen-yield-climatic-response (AHYCR) ratio

To evaluate and compare the climatic response of integrated water splitting systems, we now introduce the annual-hydrogen-yield-climatic-response (AHYCR) ratio and apply it to both our case studies. We define this value as the ratio between the real annual hydrogen yield of an outdoor-operating system ($H_{2, \text{real AY}}$) and the theoretical hydrogen yield ($H_{2 \text{ AY, STH}_{\text{std}}}$) calculated from the total integrated annual spectral irradiance impinging on the device assuming its STH efficiency at 25°C under AM1.5g illumination ($\Theta = 0^\circ$) :

$$\text{AHYCR ratio} = \frac{H_{2, \text{real AY}}}{H_{2 \text{ AY, STH}_{\text{std}}}}. \quad (16)$$

The device modelled here produces a total amount of $H_{2, \text{real AY}} = 7.84$ and $4.34 \text{ kg m}^{-2} \text{ a}^{-1}$ for the locations in southern California and Antarctica, respectively. These values are presented in blue in the first bar pair of the grouped bar chart shown in Fig. 8. From its STH efficiency of 24.58% at standard conditions (see Fig. S2 in the SI) and the total spectral irradiance of $2316.95 \text{ kWh m}^{-2} \text{ a}^{-1}$, a value for $H_{2 \text{ AY, STH}_{\text{std}}}$ of $8.71 \text{ kg m}^{-2} \text{ a}^{-1}$ can be calculated for the location in southern California. For Antarctica, the total spectral irradiance of $1272.35 \text{ kWh m}^{-2} \text{ a}^{-1}$ translates into a value of $4.78 \text{ kg m}^{-2} \text{ a}^{-1}$ for $H_{2 \text{ AY, STH}_{\text{std}}}$. These values are indicated as white bars in the first bar pair. According to our definition in equation (16), AHYCR ratios of 0.90 and 0.91 are obtained for southern California and Antarctica, respectively. In other words, the system produces around 90% of the hydrogen that would be expected from the total integrated spectral irradiance in a year assuming its STH efficiency under standard conditions for both examples locations. These AHYCR ratios are relatively high and imply that the efficiency losses in our case study are in the same range as the losses associated with power inverters (note that efficiency losses resulting from spectral mismatch would also affect the hydrogen yield when power inverters are used). Moreover, it is remarkable that the device nearly shows the same AHYCR ratio for both locations with completely different climatic conditions. This could mean that direct solar water splitting devices would not necessarily have to be customized for each production location, as it was also recently suggested for dual-junction solar cells.²⁴ However, these findings cannot be generalized yet. Further climate zones will have to be investigated and experimental data should backup the modelling since parameters as for example wind, cloud cover, potential temperature gradients in the device, the influence of a flowing electrolyte, and catalyst or membrane degradation should also be considered.

To give more examples for the application of the AHYCR ratio, we performed additional modelling with slightly changed input parameters. Recent studies from the solar water splitting community highlight the efficiency gains caused by thermal coupling of the solar cells and the electrochemical component.^{5,19,25,29} To the best of our knowledge,

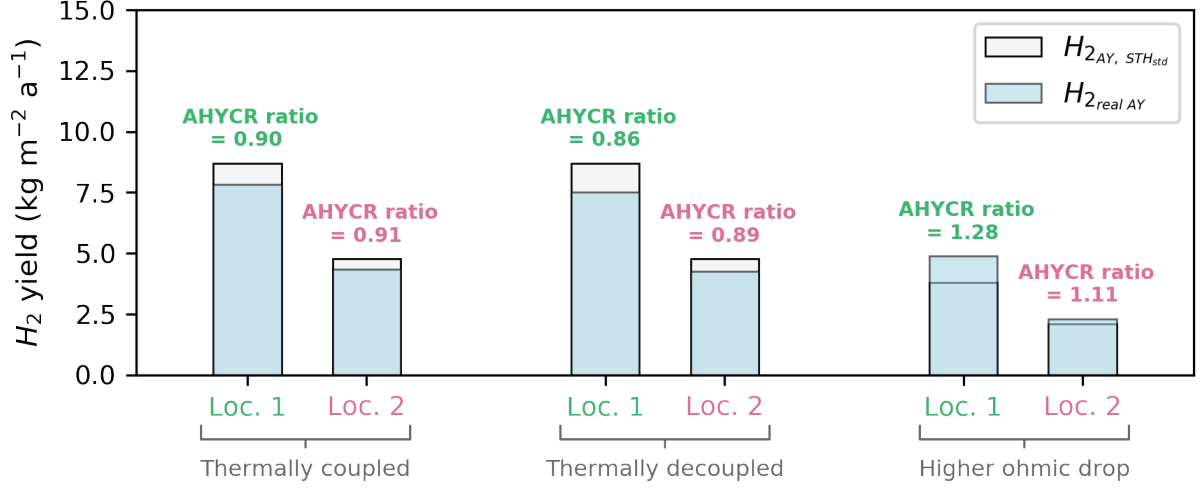


Fig. 8: Modelled $H_{2, \text{real AY}}$ and $H_{2, \text{AY, STH}_{\text{std}}}$ for the solar water splitting device operating in southern California (Location 1) and near the Neumayer station in Antarctica (Location 2) for a thermally coupled as well as decoupled configuration, and assuming higher ohmic losses in the electrolyzer. The bars are annotated with the resulting AHYCR ratios.

however, these efficiency gains were not evaluated for an outdoor-operating device exposed to changing weather conditions yet. To get a first impression, the AHYCR ratios for both locations were therefore also determined for a thermally decoupled device configuration. This means that the solar cell temperature is still estimated from the irradiance and the ambient temperature according to equation (1), whereas the electrolyzer operating temperature is assumed to follow the ambient temperature. As expected from the lower performance of the electrolyzer with decreasing temperature (lower catalytic activity and higher ohmic drop), the annual hydrogen yields for both locations are smaller than the ones obtained for the thermally coupled configuration (see second bar pair in Fig. 8). The modelled values for $H_{2, \text{real AY}}$ of 7.84 and 4.34 kg m⁻²a⁻¹ translate into AHYCR ratios of 0.86 and 0.89 for California and Antarctica, respectively. The hourly resolved modelling results are shown in Figs. S8 and S9 in the SI. For our example device, the losses in the produced hydrogen mass associated with thermal decoupling are 4.4% for California and 2.2% for Antarctica. Note that the lower losses for the operation in Antarctica do not mean that thermal coupling at low temperatures is less beneficial. This finding is mostly a result of the in general lower hourly irradiances in Antarctica (see Fig. 5), which is accompanied by a lower demand on the electrolyzer performance. Moreover, we had to use extrapolated data for the temperature-dependent characteristic of the electrolyzer for the low temperatures. For the configuration chosen here, this results in the voltage at the MPP of the solar cell as a function of the temperature following almost exactly the voltage requirement of the AEM electrolyzer. If real-world resistivities are – especially at lower temperatures as in Ref. ¹⁹ – higher, the AHYCR ratio for this location will drop and the difference of overall yearly hydrogen production between coupled and decoupled approaches can increase. In general, the AHYCR ratio strongly depends on the overall device configuration and temperature-dependent characteristics of the different components. Note that these calculations cannot be used to show the benefits of thermally coupled solar water splitting devices compared to the completely decoupled PV-electrolysis approach. Practical electrolyzers are in general compact (i.e. low area for heat dissipation) and operated at much higher current densities. Due to an operation potential beyond the thermoneutral voltage of water splitting, they heat themselves and require – dependent on the scale – cooling. Consequently, a comparison between both approaches should include the whole energy balance at different scales, which is beyond the scope of this work.

As another example, modelling for the two locations was also performed with a hypothetical, significantly increased ohmic resistance of the electrolyzer in a thermally coupled configuration. The temperature-dependent ohmic resistance and the resulting IV curves are shown in Fig. S10 and Fig. S11 in the SI, respectively. Note that the front absorber bandgap was not optimized to the lower electrolyzer performance resulting in a non-optimal operation point at standard conditions. Moreover, the chosen ohmic resistance is unrealistically large for state-of-the-art, membrane-based electrolyzers. However, relatively high ohmic resistances can for example occur in photoelectrochemical devices or membrane-free electrolyzers.⁹ The hourly resolved modelling results for both locations are shown in Fig. S12 and Fig. S13 in the SI. Due to the high ohmic losses, the coupling efficiency and the STH efficiency increase with decreasing irradiance. This is again caused by the in general lower demand on the electrolyzer performance with lower irradiances (see above). Since the denominator of the AHYCR ratio is defined as the hydrogen produced assuming STH efficiency at standard conditions (i.e. a relatively high irradiance), AHYCR ratios of higher than 1 are obtained for this device configuration. Specifically, AHYCR ratios of 1.28 and 1.11 are calculated for California and Antarctica, respectively (see third bar pair in Fig. 8). The higher AHYCR ratio for the device operating in California with subtropical climate

results from the fact that the contrasting temperature effects on the solar cell and electrolyzer IV characteristics do not cancel each other out anymore (see Fig. S11 in the SI). The decrease in the electrolyzer performance with lower temperature cannot be compensated by the higher VOC of the solar cells. Hence, the device performance suffers from lower operating temperatures and explains the lower AHYCR ratio found for Antarctica. These results show that testing of solar hydrogen devices under standard conditions can lead to both, a significant under-, but also overestimation of annual production rates at a given site.

4 Conclusions

We have modelled the climatic response of a solar water splitting device based on state-of-the-art AlGaAs//Si dual-junction solar cells and a thermally coupled AEM electrolyzer for a location in southern California and in Antarctica. Based on this, we have introduced the AHYCR ratio as a figure of merit for evaluating, comparing and optimizing the climatic response of integrated solar water splitting devices. It describes the ratio between the real annual hydrogen yield of an outdoor-operating system and the theoretical hydrogen yield calculated from the total yearly irradiance impinging on the device assuming its STH efficiency under standard conditions (AM1.5g, $T = 25^{\circ}\text{C}$, $\Theta = 0^{\circ}$). For our case study, we found a relatively high AHYCR ratio of around 0.9 for both the locations. This indicates that this exemplary device is relatively less affected by changing weather conditions and shows that it is at least in theory possible to construct systems that do not extensively suffer from non-optimal operation points. Future work, however, should be directed to not only model, but also experimentally determine the AHYCR ratio of solar water splitting devices in different climate zones. Moreover, parameters as for example wind, potential temperature gradients in the device, and catalyst as well as membrane degradation should also be considered. This would help to answer the question as to whether the efficiency losses due to potential non-optimal operation points of integrated solar water splitting devices are more severe than the efficiency losses associated with power inverters in the completely decoupled PV-electrolysis approach. Moreover, it would help to evaluate whether solar water splitting systems will have to be customized for each production location or not. Our work should stimulate the solar water splitting community to determine the AHYCR ratio of their solar water splitting devices as a figure of merit to evaluate the real-life performance.

Conflicts of interest

There are no conflicts of interest to declare.

Acknowledgements

This work was supported by the German Bundesministerium für Bildung und Forschung (BMBF), project “H2Demo” (No. 03SF0619K). M.M.M. acknowledges funding from the German Research Foundation (DFG) project number 434023472.

References

- [1] Amran Al-Ashouri, Eike Köhnen, Bor Li, Artiom Magomedov, Hannes Hempel, Pietro Caprioglio, José A. Márquez, Anna Belen Morales Vilches, Ernestas Kasparavicius, Joel A. Smith, Nga Phung, Dorothee Menzel, Max Grischek, Lukas Kegelmann, Dieter Skroblin, Christian Gollwitzer, Tadas Malinauskas, Marko Jošt, Gašper Matič, Bernd Rech, Rutger Schlatmann, Marko Topič, Lars Korte, Antonio Abate, Bernd Stannowski, Dieter Neher, Martin Stoltterfoht, Thomas Unold, Vytautas Getautis, and Steve Albrecht. Monolithic perovskite/silicon tandem solar cell with $> 29\%$ efficiency by enhanced hole extraction. *Science*, 370(6522):1300–1309, 2020.
- [2] Alexandre W. Walker, Jeffrey F. Wheeldon, Olivier Thériault, Mark D. Yandt, Karin Hinzer, 37th IEEE Photovoltaic Specialists Conference. DOI: 10.1109/PVSC.2011.6186018, 2011.
- [3] İlknur Bayrak Pehlivan, Ulf Malm, Peter Neretnieks, Andreas Glüsen, Martin Müller, Katharina Welter, Stefan Haas, Sonya. Calnan, Andrea. Canino, Rachela G. Milazzo, Stefania M. S. Privitera, Salvatore A. Lombardo, Lars Stolt, Marika Edoff, and Tomas Edvinsson. The climatic response of thermally integrated photovoltaic–electrolysis water splitting using Si and CIGS combined with acidic and alkaline electrolysis. *Sustainable Energy Fuels*, 4(12):6011–6022, 2020.
- [4] Carlos F. Blanco, Stefano Cucurachi, Frank Dimroth, Jeroen B. Guinée, Willie J. G. M. Peijnenburg, and Martina G. Vijver. Environmental impacts of III–V/silicon photovoltaics: life cycle assessment and guidance for sustainable manufacturing. *Energy Environ. Sci.*, 13:4280–4290, 2020.

- [5] Sonya Calnan, Rory Bagacki, Fuxi Bao, Iris Dorbandt, Erno Kemppainen, Christian Schary, Rutger Schlatmann, Marco Leonardi, Salvatore A. Lombardo, R. Gabriella Milazzo, Stefania M. S. Privitera, Fabrizio Bizzarri, Carmelo Connelly, Daniele Consoli, Cosimo Gerardi, Pierenrico Zani, Marcelo Carmo, Stefan Haas, Minoh Lee, Martin Mueller, Walter Zwaygardt, Johan Oscarsson, Lars Stolt, Marika Edoff, Tomas Edvinsson, and Ilknur Bayrak Pehlivan. Development of various photovoltaic-driven water electrolysis technologies for green solar hydrogen generation. *Sol. RRL*, page 2100479, 2021.
- [6] Romain Cariou, Jan Benick, Frank Feldmann, Oliver Höhn, Hubert Hauser, Paul Beutel, Nasser Razek, Markus Wimplinger, Benedikt Bläsi, David Lackner, Martin Hermle, Gerald Siefer, Stefan W. Glunz, Andreas W. Bett, and Frank Dimroth. III–V-on-silicon solar cells reaching 33% photoconversion efficiency in two-terminal configuration. *Nat. Energy*, 3(4):326–333, 2018.
- [7] Wen-Hui Cheng, Matthias H. Richter, Matthias M. May, Jens Ohlmann, David Lackner, Frank Dimroth, Thomas Hannappel, Harry A. Atwater, and Hans-Joachim Lewerenz. Monolithic photoelectrochemical device for direct water splitting with 19% efficiency. *ACS Energy Lett.*, 3(8):1795–1800, 2018.
- [8] Claudia Emde, Robert Buras-Schnell, Arve Kylling, Bernhard Mayer, Josef Gasteiger, Ulrich Hamann, Jonas Kylling, Bettina Richter, Christian Pause, Timothy Dowling, and Luca Bugliaro. The libRadtran software package for radiative transfer calculations (version 2.0.1). *Geosci. Model Dev.*, 9(5):1647–1672, 2016.
- [9] Daniel V. Esposito. Membraneless electrolyzers for low-cost hydrogen production in a renewable energy future. *Joule*, 1(4):651–658, 2017.
- [10] Sophia Haussener, Shu Hu, Chengxiang Xiang, Adam Z. Weber, and Nathan S. Lewis. Simulations of the irradiation and temperature dependence of the efficiency of tandem photoelectrochemical water-splitting systems. *Energy Environ. Sci.*, 6:3605–3618, 2013.
- [11] William F. Holmgren, Clifford W. Hansen, and Mark A. Mikofski. Pvlb python: a python package for modeling solar energy systems. *J. Open Source Softw.*, 3(29):884, 2018.
- [12] Oliver Höhn, Jayanth N. Murthy, Marc Steiner, Nico Tucher, Elke Lorenz, Jan Christoph Goldschmidt, Frank Dimroth, and Benedikt Bläsi. Impact of irradiance data on the energy yield modeling of dual-junction solar module stacks for one-sun applications. *IEEE J. Photovolt.*, 11(3):692–698, 2021.
- [13] Maximilian T. Hörantner, Tomas Leijtens, Mark E. Ziffer, Giles E. Eperon, M. Greyson Christoforo, Michael D. McGehee, and Henry J. Snaith. The potential of multijunction perovskite solar cells. *ACS Energy Lett.*, 2(10):2506–2513, 2017.
- [14] Maximilian T. Hörantner and Henry J. Snaith. Predicting and optimising the energy yield of perovskite-on-silicon tandem solar cells under real world conditions. *Energy Environ. Sci.*, 10:1983–1993, 2017.
- [15] Jieyang Jia, Linsey C. Seitz, Jesse D. Benck, Yijie Huo, Yusi Chen, Jia Wei Desmond Ng, Taner Bilir, James S. Harris, and Thomas F. Jaramillo. Solar water splitting by photovoltaic-electrolysis with a solar-to-hydrogen efficiency over 30%. *Nat. Commun.*, 7(1):13237, 2016.
- [16] Joaquín Muñoz Sabater, ERA5-Land hourly data from 1981 to present. Copernicus Climate Change Service (C3S) Climate Data Store (CDS). 10.24381/cds.e2161bac, 2015. Accessed: 2022-03-02.
- [17] Erno Kemppainen, Stefan Aschbrenner, Fuxi Bao, Aline Luxa, Christian Schary, Radu Bors, Stefan Janke, Iris Dorbandt, Bernd Stannowski, Rutger Schlatmann, and Sonya Calnan. Effect of the ambient conditions on the operation of a large-area integrated photovoltaic-electrolyser. *Sustainable Energy Fuels*, 4:4831–4847, 2020.
- [18] Eike Köhnen, Marko Jošt, Anna Belen Morales-Vilches, Philipp Tockhorn, Amran Al-Ashouri, Bart Macco, Lukas Kegelmann, Lars Korte, Bernd Rech, Rutger Schlatmann, Bernd Stannowski, and Steve Albrecht. Highly efficient monolithic perovskite silicon tandem solar cells: analyzing the influence of current mismatch on device performance. *Sustainable Energy Fuels*, 3:1995–2005, 2019.
- [19] Moritz Kölbach, Kira Rehfeld, and Matthias M. May. Efficiency gains for thermally coupled solar hydrogen production in extreme cold. *Energy Environ. Sci.*, 14:4410–4417, 2021.
- [20] Matthias M. May, Moritz Kölbach, YaSoFo - Yet Another SOLar Fuels Optimizer. Zenodo. DOI: 10.5281/zenodo.1489157, 2022.
- [21] Matthias M. May, David Lackner, Jens Ohlmann, Frank Dimroth, Roel van de Krol, Thomas Hannappel, and Klaus Schwarzburg. On the benchmarking of multi-junction photoelectrochemical fuel generating devices. *Sustainable Energy Fuels*, 1:492–503, 2017.

- [22] Bernhard Mayer. Radiative transfer in the cloudy atmosphere. *EPJ Web Conf.*, 1:75–99, 2009.
- [23] Bernhard Mayer and Arve Kylling. Technical note: The libRadtran software package for radiative transfer calculations - description and examples of use. *Atmos. Chem. Phys.*, 5(7):1855–1877, 2005.
- [24] Oliver Höhn, Mario Hanser, Marc Steiner, Elke Lorenz, Benedikt Bläsi, Stefan W. Glunz, Frank Dimroth, 38th European PV Solar Energy Conference and Exhibition. DOI: 10.4229/EUPVSEC20212021-3BV.2.66, 2021.
- [25] İlknur Bayrak Pehlivan, Johan Oscarsson, Zhen Qiu, Lars Stolt, Marika Edoff, and Tomas Edvinsson. NiMoV and NiO-based catalysts for efficient solar-driven water splitting using thermally integrated photovoltaics in a scalable approach. *iScience*, 24(1):101910, 2021.
- [26] Markus Reuß, Julian Reul, Thomas Grube, Manuel Langemann, Sonya Calnan, Martin Robinius, Rutger Schlattermann, Uwe Rau, and Detlef Stolten. Solar hydrogen production: a bottom-up analysis of different photovoltaic-electrolysis pathways. *Sustainable Energy Fuels*, 3:801–813, 2019.
- [27] Priyanka Singh, S.N. Singh, M. Lal, and M. Husain. Temperature dependence of I–V characteristics and performance parameters of silicon solar cell. *Sol. Energy Mater. Sol. Cells*, 92(12):1611–1616, 2008.
- [28] Kevin Sivula and Roel van de Krol. Semiconducting materials for photoelectrochemical energy conversion. *Nat. Rev. Mater.*, 1(2):15010, 2016.
- [29] Saurabh Tembhurne, Fredy Nandjou, and Sophia Haussener. A thermally synergistic photo-electrochemical hydrogen generator operating under concentrated solar irradiation. *Nat. Energy*, 4(5):399–407, 2019.
- [30] Nico Tucher, Johannes Eisenlohr, Habtamu Gebrewold, Peter Kiefel, Oliver Höhn, Hubert Hauser, Jan Christoph Goldschmidt, and Benedikt Bläsi. Optical simulation of photovoltaic modules with multiple textured interfaces using the matrix-based formalism OPTOS. *Opt. Express*, 24(14):A1083–A1093, 2016.
- [31] Nico Tucher, Johannes Eisenlohr, Peter Kiefel, Oliver Höhn, Hubert Hauser, Marius Peters, Claas Müller, Jan Christoph Goldschmidt, and Benedikt Bläsi. 3D optical simulation formalism OPTOS for textured silicon solar cells. *Opt. Express*, 23(24):A1720–A1734, 2015.
- [32] Falko Ueckerdt, Christian Bauer, Alois Dirnreichner, Jordan Everall, Romain Sacchi, and Gunnar Luderer. Potential and risks of hydrogen-based e-fuels in climate change mitigation. *Nat. Clim. Change*, 11(5):384–393, 2021.
- [33] Y.P. Varshni. Temperature dependence of the energy gap in semiconductors. *Physica*, 34(1):149–154, 1967.
- [34] Immanuel Vincent, Eun-Chong Lee, and Hyung-Man Kim. Comprehensive impedance investigation of low-cost anion exchange membrane electrolysis for large-scale hydrogen production. *Sci. Rep.*, 11(1):293, 2021.
- [35] I. Vurgaftman, J. R. Meyer, and L. R. Ram-Mohan. Band parameters for III–V compound semiconductors and their alloys. *J. Appl. Phys.*, 89(11):5815–5875, 2001.
- [36] M.W. Wanlass, K.A. Emery, T.A. Gessert, G.S. Horner, C.R. Osterwald, and T.J. Coutts. Practical considerations in tandem cell modeling. *Sol. Cells*, 27(1):191–204, 1989.
- [37] Katharina Welter, Jan-Philipp Becker, Friedhelm Finger, Wolfram Jaegermann, and Vladimir Smirnov. Performance of integrated thin-film silicon solar cell-based water-splitting devices under varying illumination angles and an estimation of their annual hydrogen production. *Energy Fuels*, 35(1):839–846, 2021.
- [38] Katharina Welter, Vladimir Smirnov, Jan-Philipp Becker, Patrick Borowski, Sascha Hoch, Artjom Maljusch, Wolfram Jaegermann, and Friedhelm Finger. The influence of operation temperature and variations of the illumination on the performance of integrated photoelectrochemical water-splitting devices. *ChemElectroChem*, 4(8):2099–2108, 2017.
- [39] Yu Xie and Manajit Sengupta. A fast all-sky radiation model for solar applications with narrowband irradiances on tilted surfaces (FARMS-NIT): Part I. The clear-sky model. *Sol. Energy*, 174:691–702, 2018.
- [40] Yu Xie, Manajit Sengupta, and Mike Dooraghi. Assessment of uncertainty in the numerical simulation of solar irradiance over inclined PV panels: New algorithms using measurements and modeling tools. *Sol. Energy*, 165:55–64, 2018.
- [41] Yu Xie, Manajit Sengupta, and Chenxi Wang. A fast all-sky radiation model for solar applications with narrowband irradiances on tilted surfaces (FARMS-NIT): Part II. the cloudy-sky model. *Sol. Energy*, 188:799–812, 2019.

Supporting information

The annual-hydrogen-yield-climatic-response ratio: evaluating the real-life performance of integrated solar water splitting devices

Moritz Kölbach,^{*a,b,c} Oliver Höhn,^d Kira Rehfeld,^e Manuel Finkbeiner,^f James Barry,^{f,g} and Matthias M. May^{a,b}

^aUniversität Tübingen, Institute of Physical and Theoretical Chemistry, Tübingen, Germany.

^bUniversität Ulm, Institute of Theoretical Chemistry, Ulm, Germany.

^cHelmholtz-Zentrum Berlin für Materialien und Energie GmbH, Institute for Solar Fuels, Berlin, Germany.

^dFraunhofer ISE für Solare Energiesysteme, Freiburg, Germany.

^eUniversität Tübingen, Department of Geosciences and Department of Physics, Tübingen, Germany.

^fUniversität Heidelberg, Institute of Environmental Physics, Heidelberg, Germany.

^gInternational Centre for Sustainable Development, Hochschule Bonn-Rhein-Sieg, Sankt Augustin, Germany.

*Email Address: moritz.koelbach@uni-tuebingen.de

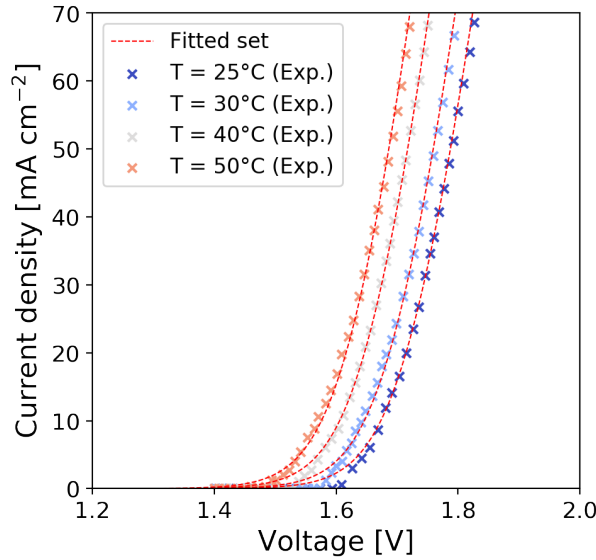


Fig. S1: Fitted set of temperature-dependent experimental IV curves of an AEM electrolyzer^[1] using the routine described in the manuscript.

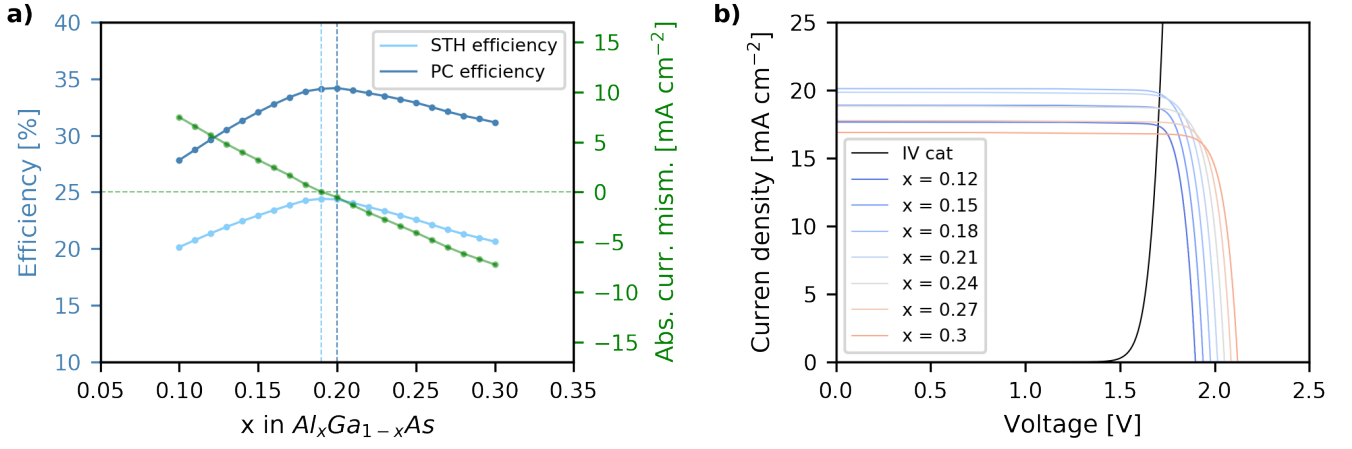


Fig. S2: (a) Left y-axis: STH and photoconversion (PC) efficiency as a function of the x in the $\text{Al}_x\text{Ga}_{1-x}\text{As}$ top absorber for a device operating temperature of 25°C under AM1.5g illumination. The efficiency maxima are indicated as vertical dashed lines. Right y-axis: Corresponding absolute current mismatch in the dual-junction. (b) Corresponding IV characteristics of the AEM electrolyzer and the solar cell for exemplary top absorber compositions.

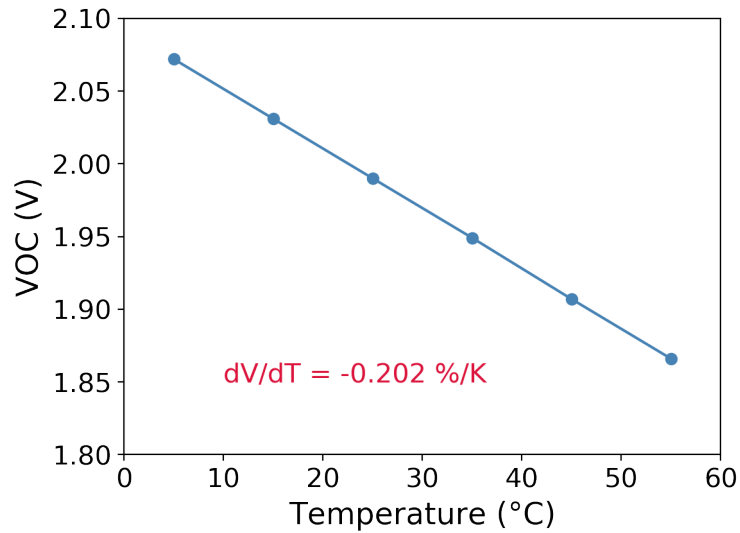


Fig. S3: Modelled open circuit voltage of the AlGaAs/Si dual-junction as a function of the temperature. A VOC temperature coefficient of $-0.202 \text{ \%}/\text{K}$ can be extracted.

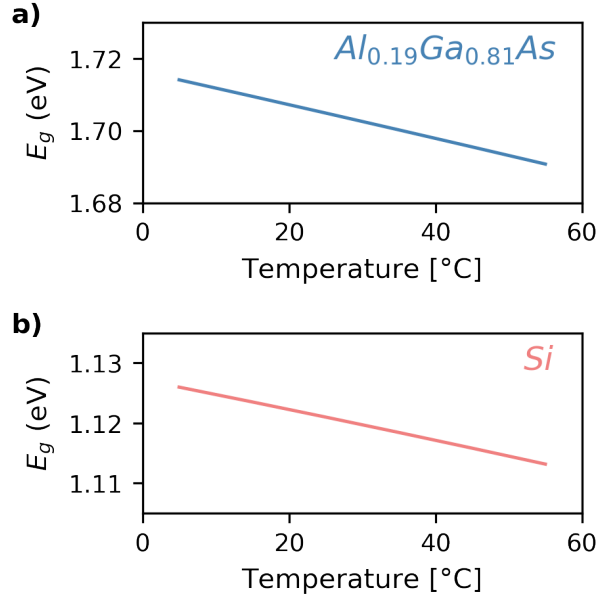


Fig. S4: Temperature dependence of the bandgap of (a) AlGaAs and (b) Si.

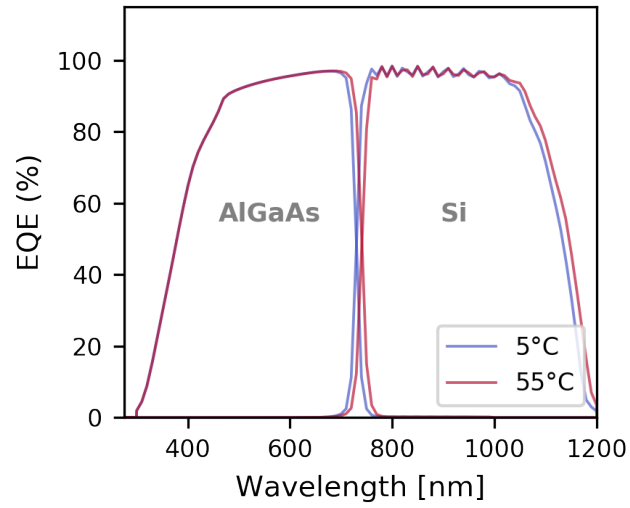


Fig. S5: Modelled external quantum efficiency of the AlGaAs top and Si bottom absorber for a temperature of 5°C and 55°C assuming an incidence angle of 0°.

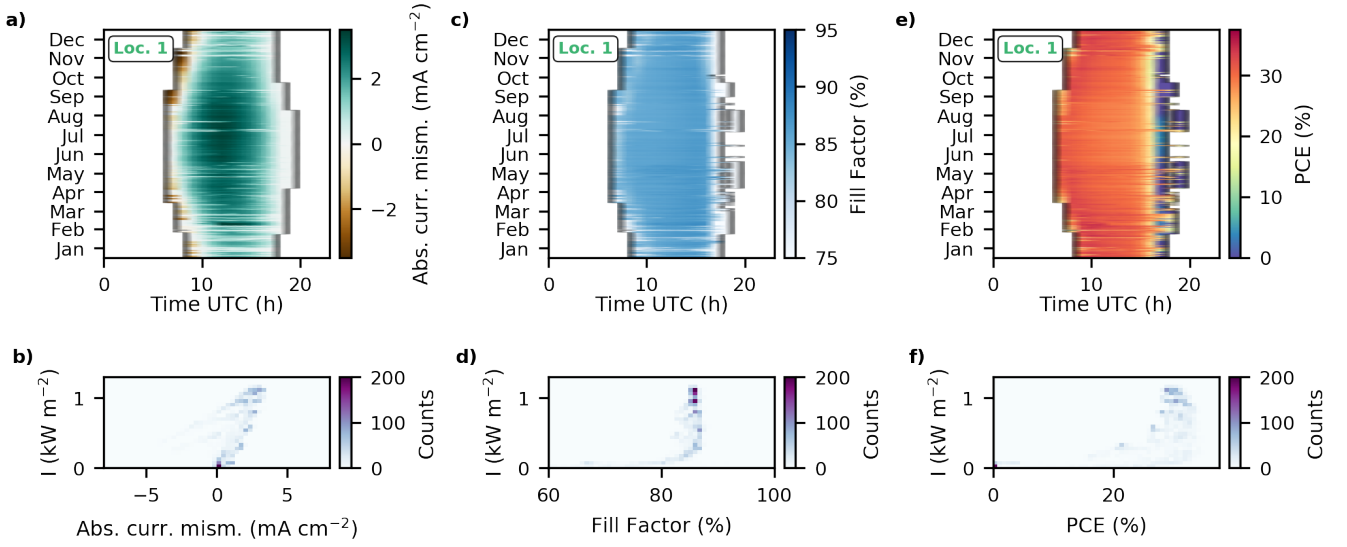


Fig. S6: Modelled climatic response of the AlGaAs//Si dual-junction for the location in southern California. (a) Hourly resolved annual absolute current mismatch in the dual-junction. (b) 2D histogram of the absolute current mismatch with regard to the total spectral irradiance impinging on the device. (c) Hourly resolved annual fill factor of the dual-junction. (d) 2D histogram of the fill factor and the total spectral irradiance. (e) Hourly resolved annual photoconversion efficiency (PCE). (f) 2D histogram of the PCE and the total spectral irradiance.

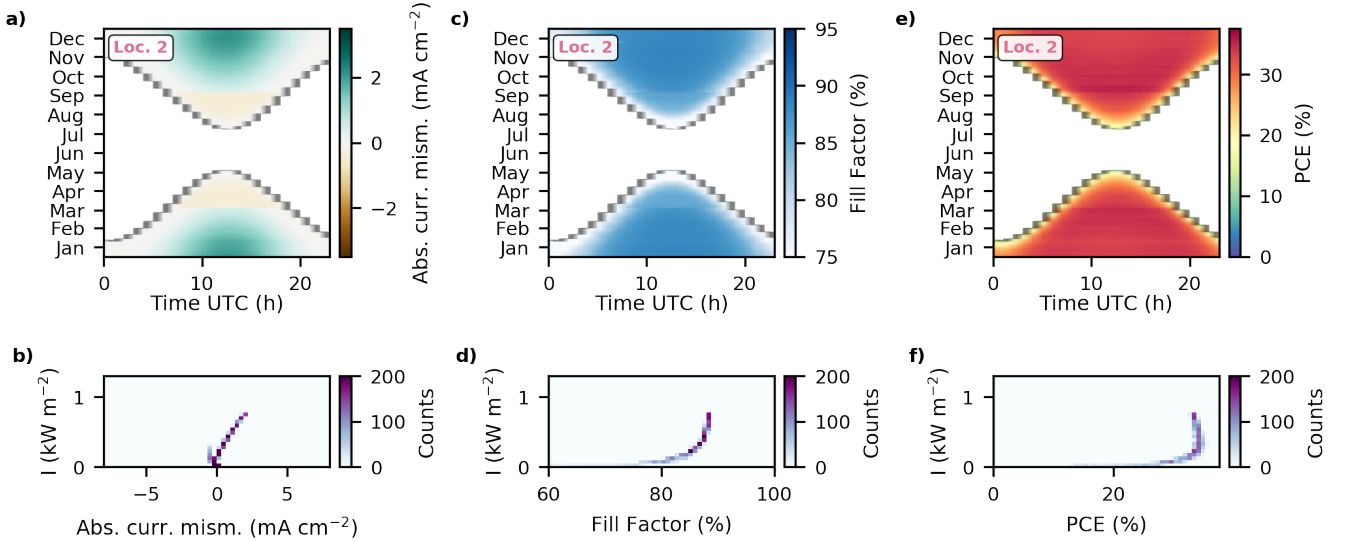


Fig. S7: Modelled climatic response of the AlGaAs//Si dual-junction in Antarctica. (a) Hourly resolved annual absolute current mismatch in the dual-junction. (b) 2D histogram of the absolute current mismatch with regard to the total spectral irradiance impinging on the device. (c) Hourly resolved annual fill factor of the dual-junction. (d) 2D histogram of the fill factor and the total spectral irradiance. (e) Hourly resolved annual PCE. (f) 2D histogram of the PCE and the total spectral irradiance.

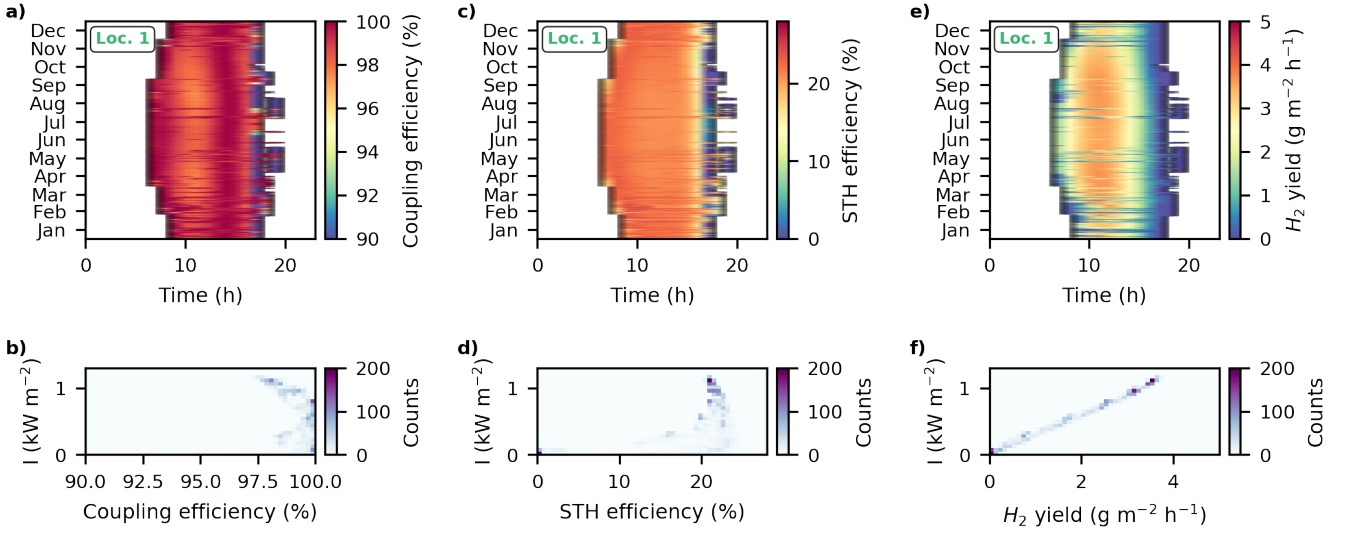


Fig. S8: Modelled climatic response of the solar water splitting device based on an AlGaAs//Si dual-junction and an AEM electrolyzer for the location in southern California for a thermally decoupled configuration. (a) Hourly resolved annual coupling efficiency. (b) 2D histogram of the coupling efficiency with regard to the total spectral irradiance impinging on the device. (c) Hourly resolved annual STH efficiency. (d) 2D histogram of the STH efficiency and the total spectral irradiance. (e) Hourly resolved annual hydrogen yield. (f) 2D histogram of the hydrogen yield and the total spectral irradiance.

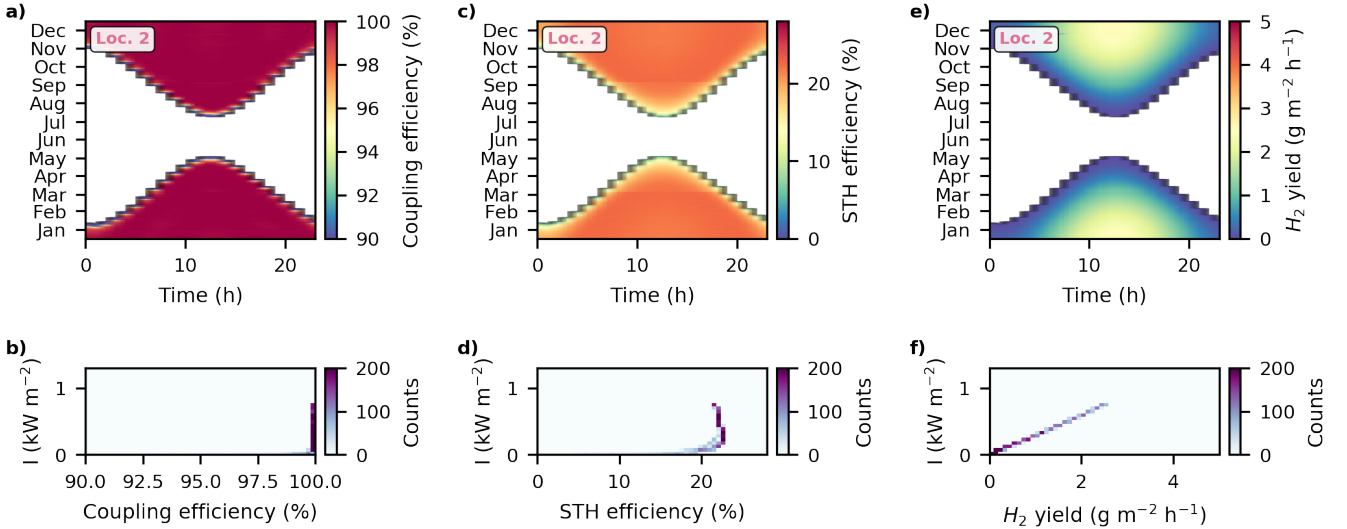


Fig. S9: Modelled climatic response of the solar water splitting device based on an AlGaAs//Si dual-junction and an AEM electrolyzer for the location in Antarctica for a thermally decoupled configuration. (a) Hourly resolved annual coupling efficiency. (b) 2D histogram of the coupling efficiency with regard to the total spectral irradiance impinging on the device. (c) Hourly resolved annual STH efficiency. (d) 2D histogram of the STH efficiency and the total spectral irradiance. (e) Hourly resolved annual hydrogen yield. (f) 2D histogram of the hydrogen yield and the total spectral irradiance.

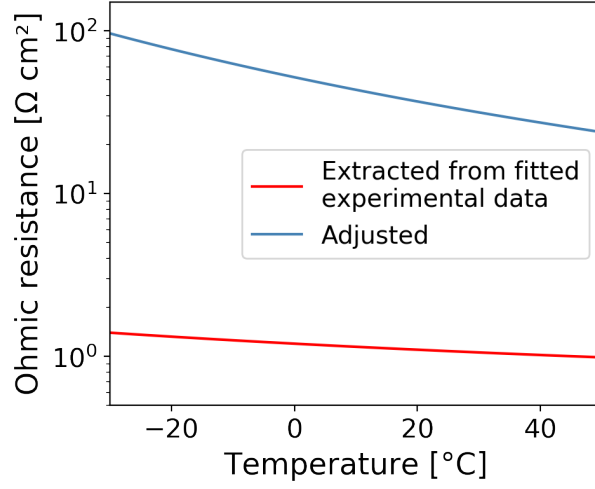


Fig. S10: Ohmic cell resistance of the electrolyzer as a function of its operating temperature. Red curve: Extracted resistance from the fitted set of temperature-dependent experimental IV curves (see Figure S1 and Table 2 in the manuscript). Blue curve: Resistance used for the reference modelling with a higher ohmic drop shown in the right bar pair of Figure 8 in the manuscript. To increase the resistance, a membrane activation energy $E_{a, \text{mem}}$ of 11.4 kJ mol^{-1} was assumed.

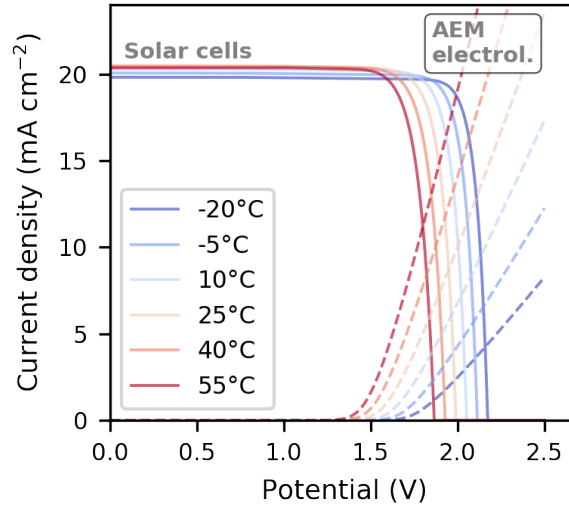


Fig. S11: Influence of the operating temperature on the IV characteristics of the AlGaAs//Si dual-junction and the AEM electrolyzer assuming the higher ohmic resistance as shown in Figure S10. The solar cell IV curves were modelled assuming AM1.5g illumination and an angle of incidence equal to 0° . An STH efficiency of 10.76% can be extracted for a temperature of 25°C .

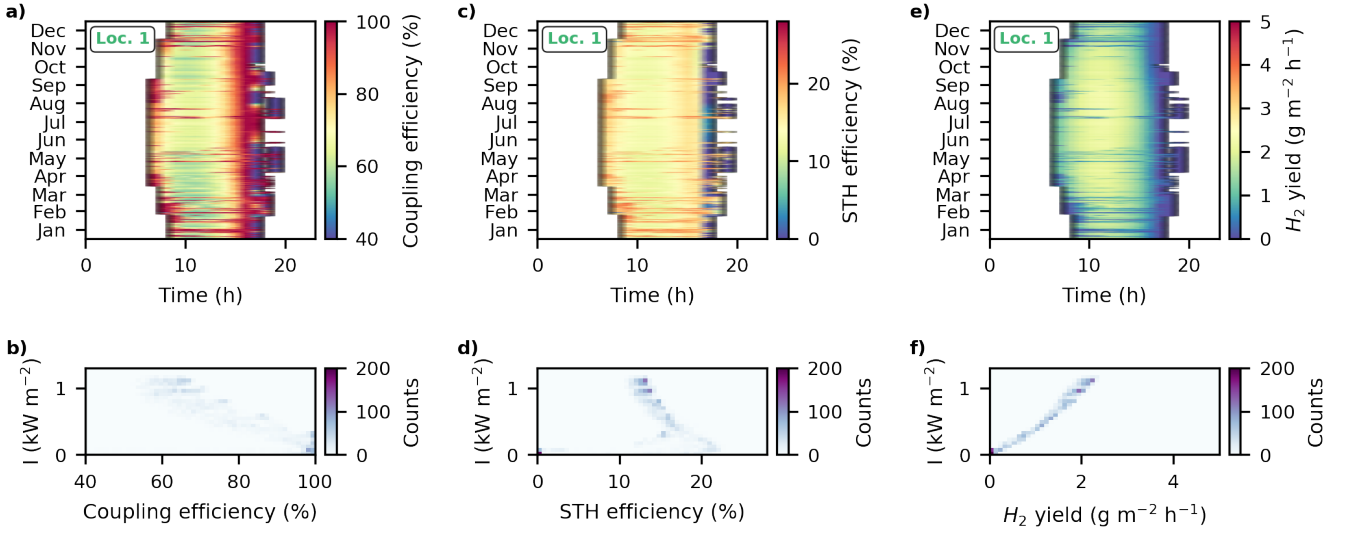


Fig. S12: Modelled climatic response of the solar water splitting device based on an AlGaAs//Si dual-junction and an AEM electrolyzer with a higher ohmic resistance (see Figure S10 and S11) for the location in southern California. (a) Hourly resolved annual coupling efficiency. (b) 2D histogram of the coupling efficiency with regard to the total spectral irradiance impinging on the device. (c) Hourly resolved annual STH efficiency. (d) 2D histogram of the STH efficiency and the total spectral irradiance. (e) Hourly resolved annual hydrogen yield. (f) 2D histogram of the hydrogen yield and the total spectral irradiance.

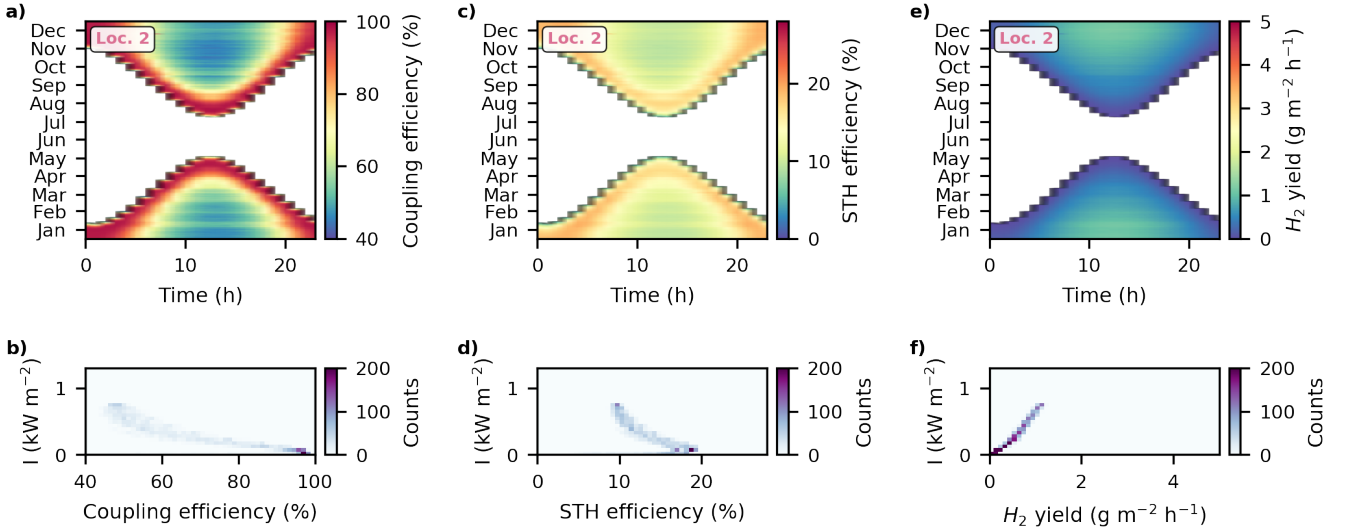


Fig. S13: Modelled climatic response of the solar water splitting device based on an AlGaAs//Si dual-junction and an AEM electrolyzer with a higher ohmic resistance (see Figure S10 and S11) for the location in Antarctica. (a) Hourly resolved annual coupling efficiency. (b) 2D histogram of the coupling efficiency with regard to the total spectral irradiance impinging on the device. (c) Hourly resolved annual STH efficiency. (d) 2D histogram of the STH efficiency and the total spectral irradiance. (e) Hourly resolved annual hydrogen yield. (f) 2D histogram of the hydrogen yield and the total spectral irradiance.

References

- [1] Immanuel Vincent, Eun-Chong Lee, and Hyung-Man Kim. Comprehensive impedance investigation of low-cost anion exchange membrane electrolysis for large-scale hydrogen production. *Sci. Rep.*, 11(1):293, 2021.